SCIPEDIA Revista Internacional de Métodos Numéricos para Cálculo y Diseño en Ingeniería

Revista Internacional Métodos numéricos para cálculo y diseño en ingeniería RIMNI In cooperation with CIMNE

Multi-Objective Optimization and Performance Evaluation of Manifold-Based Cooling Systems for Battery Thermal Management Using RSM and NSGA-II

Hanwen Zhang[1], Poo Balan Ganesan[1,2,*], Wen Tong Chong[1,2] and Mohd Nashrul Bin Mohd Zubir[1]

[1]Department of Mechanical Engineering, Faculty of Engineering, Universiti Malaya, Kuala Lumpur, 50603, Malaysia

[2]Center for Energy Sciences (CES), Universiti Malaya, Kuala Lumpur, 50603, Malaysia

ABSTRACT

Efficient thermal management is critical to the safety, performance, and longevity of lithium-ion battery (LIB) energy storage systems. In this study, a novel manifold cold plate featuring an overflow channel with a triangular ridge at the bottom is proposed for a liquid-cooled Battery Thermal Management System (BTMS). A comprehensive multi-objective optimization framework is developed by integrating Response Surface Methodology (RSM), the Non-dominated Sorting Genetic Algorithm II (NSGA-II), and the Linear Programming Technique for Multidimensional Analysis of Preference (LINMAP) decision-making method to minimize the maximum temperature difference (ΔT_{cell}) and pressure drop (ΔP) across the cooling plate. The design variables include the manifold channel width ratio (λ), the height ratio (ϕ), the inlet velocity (u), and the triangular ridge angle (θ). Second-order polynomial regression models are constructed and validated using Analysis of Variance (ANOVA), yielding high coefficients of determination ($R^2 = 0.9926$ for ΔT_{cell} and 0.9600 for ΔP), confirming strong predictive accuracy. Sensitivity analysis reveals that the inlet velocity and channel angle are the primary factors influencing system performance. The LINMAP-based decision-making approach identifies an optimal configuration with $\lambda = 1.031$, $\phi = 1.47$, $u = 1.671$ m/s, and $\theta = 29.8°$, achieving a ΔT_{cell} of 12.61°C and a ΔP of 6742.99 Pa, with validation errors below 3%. Transient simulations at 0.5 and 1C discharge rates show that the LINMAP-optimized design reduces the maximum cell temperature by 13.12°C and 11.77°C, respectively, compared to the natural convection baseline, and by 1.42°C and 0.76°C compared to the prototype design, while maintaining comparable hydraulic resistance. This work offers valuable guidance for designing and optimizing liquid-cooled battery thermal management systems with complex manifold structures.

OPEN ACCESS

Received: 20/06/2025

Accepted: 30/07/2025

Published: 23/01/2026

DOI
10.23967/j.rimni.2025.10.69320

Keywords:
Battery thermal management
response surface methodology
multi-objective optimization
NSGA-II

Nomenclature/Abbreviations

Nomenclature

ΔP	Pressure drop
ΔT_{cell}	Maximum temperature difference between battery cells
λ	Inlet-to-outlet width ratio of the manifold channel

*Correspondence: Poo Balan Ganesan (poo_ganesan@um.edu.my).

ϕ	The height ratio between the manifold and overflow channels
u	Inlet velocity
θ	Triangular ridge angle
R^2	Coefficient of determination, indicating the goodness of fit of the regression model
l_b	Length of battery cell
w_b	Width of battery cell
h_b	Height of battery cell
h_o	Height of the overflow channel
w_o	Width of the overflow channel
h_m	Height of the manifold channel
w_m	Width of the manifold channel
ρ	Density
g	Gravity
E	Energy
μ	Dynamic viscosity
k	Thermal conductivity
h	Enthalpy
J	Diffusion flux
S	Source term
Q_b	Heat generated by the battery
T	Temperature
t	Time
c_p	Specific heat capacity
V_{oc}	Open-circuit voltage
I	Current
R_i	Internal resistance
d_{i+}	Euclidean distance between solution i and the ideal point
F_{ij}	Normalized value of the j_{th} objective for the i_{th} solution
F_j^{ideal}	Ideal value of the j_{th} objective among all solutions
j	Index of the j_{th} objective function
i	Index of the i_{th} solution in the Pareto front
i_{LIN}	Index of the optimal solution selected by the LINMAP decision-making method
η_c	Crossover distribution index
η_m	Mutation distribution index

Abbreviations

BTMS	Battery Thermal Management System
LIB	Lithium-ion Battery
RSM	Response Surface Methodology
NSGA-II	Non-dominated Sorting Genetic Algorithm II
LINMAP	Linear Programming Technique for Multidimensional Analysis of Preference
DoD	Depth of Discharge
ANOVA	Analysis of Variance
CCD	Central Composite Design
UDF	User-Defined Function
CFD	Computational Fluid Dynamics

1 Introduction

To address the challenges of climate change and carbon emissions, the global energy structure is undergoing a rapid transition toward renewable energy dominance [1,2]. Although green energy sources such as wind and solar power are clean and sustainable, their inherently intermittent and fluctuating output makes them challenging to integrate directly into power grid operations [3,4]. Therefore, to ensure a stable energy supply and maintain grid load balance, the development of efficient and reliable energy storage systems has become a critical enabler for achieving sustainable energy systems [5,6].

Among current mainstream energy storage technologies, LIBs have been widely deployed in large-scale electrochemical energy storage systems due to their high energy density, rapid response capabilities, and flexibility in design [7,8]. However, during high-rate charging or discharging or under elevated temperature conditions, LIBs generate significant heat [9]. If this heat is not dissipated efficiently and promptly, it can lead to performance degradation, reduced cycle life, and, in severe cases, thermal runaway and safety hazards. Therefore, the development of an efficient BTMS has become a critical aspect of LIB-based energy storage system design. Recent studies have shown that LIBs typically operate safely within a temperature range of 0°C to 45°C, with optimal electrochemical performance achieved between 15°C and 35°C [10–12]. As such, it is essential to design thermal management systems capable of maintaining the battery temperature within this optimal or acceptable range, thereby ensuring the safety, reliability, and long-term efficiency of energy storage systems.

To ensure high-efficiency, controllable, and safe operation of LIBs, extensive research has been conducted on various thermal management systems, including air cooling [13–16], liquid cooling [17–19], phase change material cooling [20–22], and heat pipes [23,24]. Among these, liquid cooling has emerged as the mainstream approach for lithium-ion battery (LIB) thermal management, owing to its superior heat transfer capability and high temperature control accuracy. Akbarzadeh et al. [25] demonstrated that, under comparable power consumption (0.5 W), liquid cooling systems can reduce battery module temperatures by approximately 3°C compared to air cooling, while also exhibiting lower temperature fluctuations and better thermal uniformity. Liquid cooling systems are generally categorized into two types: direct liquid cooling and indirect liquid cooling. In direct liquid cooling, the coolant is in direct contact with the battery casing, which enables high heat transfer efficiency [26]. However, this approach carries risks such as electrolyte leakage and insulation failure. In contrast, indirect liquid cooling transfers heat from the battery to the coolant via intermediate heat exchange components such as cold plates. Although this method introduces slightly higher thermal resistance, it offers enhanced safety, better adaptability, and has become the prevailing solution in current battery thermal management applications [27].

In indirect liquid cooling systems, the structural design of cold plates or cooling channels is a key factor determining the thermal performance and energy efficiency of the system. Extensive numerical and experimental studies have been conducted to evaluate the heat transfer effectiveness and energy consumption characteristics of indirect liquid-cooled thermal management systems for LIBs. Qian et al. [28] developed a BTMS using a cold plate with parallel and equidistant channels. They conducted numerical studies to investigate the effects of channel number, volume flow rate, and flow direction on temperature rise and distribution; the results indicated that the cooling impact improved with an increase in the inlet flow rate. Additionally, they examined a single-inlet, single-outlet, multi-channel cold plate. The numerical results demonstrated that the cooling effect increased with the number of channels. However, when the cooling channel exceeded five, the increase in the cooling impact became insignificant. Han et al. [29] numerically evaluated dielectric fluid immersion cooling

with different fin structures for LIB packs. They found that triangular fins offered the best cooling performance, reducing the maximum temperature by 4.45% and achieving the highest Nusselt number and Performance Evaluation Criterion. An optimal A/B ratio of 4.304 was identified for enhanced thermal–hydraulic efficiency. Xu et al. [27] developed an F2-type liquid cooling BTMS with an M-mode arrangement of cooling plates, designed explicitly for high-energy-density prismatic lithium-ion battery packs. The system was experimentally demonstrated to maintain effective temperature control under 1C charge-discharge conditions. The results indicated that this design outperformed other liquid cooling strategies in terms of cooling efficiency and overall heat transfer performance. Additionally, the optimal inlet temperature was found to be approximately 18.75°C, and the minimum required coolant flow rates were 6 and 12 L/h for 1 and 2C discharge rates, respectively. Wang et al. [30] proposed a modular liquid-cooled BTMS for cylindrical LIBs using a sandwich structure with integrated cooling plates. Experimental results showed that the system effectively maintained cell temperatures below 45°C under 3C discharge, with a maximum temperature difference of less than 5°C. They also demonstrated scalability by testing single and multiple module setups, indicating reliable cooling performance across various configurations. Zhang et al. [31] designed a cold plate with variable cross-sectional channels and investigated its cooling performance on rectangular LIBs. The primary focus of their analysis was to examine the impact of the channel outlet aspect ratio, flow rate, and manifolding structure on the cold plate's heat dissipation performance. Their findings demonstrated that using channels with varying cross-sections can significantly improve cooling efficiency and temperature uniformity. Jarrett et al. [32] analyzed a serpentine channel by modeling and numerically studying design variables, including length, width, and channel route. Their analysis was based on fixed boundary conditions and objective functions of average temperature, pressure drop, and temperature uniformity. They found that a single design could meet the pressure and average temperature objectives at the expense of temperature uniformity. Although substantial progress has been made, the intricate nature of these advanced cold plate structures poses considerable obstacles to real-world application [33].

Recent studies have shown the effectiveness of integrated optimization strategies in improving battery thermal and energy performance [34]. For example, Li et al. [35] proposed a multi-horizon model predictive control framework that simultaneously optimizes battery degradation, cooling energy, and traction power in connected electric vehicles. Their approach reformulates conflicting objectives into a degradation-centric function, achieving significant reductions in battery aging and energy consumption. Various multi-objective optimization methods can be employed to simultaneously improve the thermal efficiency and flow characteristics of liquid-cooled BTMSs [33,36,37]. Wanittansirichok et al. [38] applied multi-objective topology optimization to design cooling plates for liquid-based BTMS. Their study integrated a lumped battery model and assessed heat generation at C-rates ranging from 1 to 3C, achieving a deviation of less than 2% from experimental results. The optimized model reduced pressure drop by 20%–40% and lowered the maximum temperature by up to 14 K compared to the benchmark. It demonstrated effectiveness across various charge rates, offering a reliable cooling solution for EV batteries. Feng et al. [39] proposed a gradient distributed Tesla cold plate for battery module thermal management. They conducted a multi-objective optimization to improve thermal performance and energy efficiency, considering variables like mass flow rate, channel depth, and Tesla valve distance. The optimization reduced the pressure drop by 75.7% and improved temperature uniformity, with a maximum temperature difference of less than 4°C. The optimal configuration strikes a balance between high heat transfer and low energy consumption, offering a significant reduction in both thermal performance and pressure drop. Zhu et al. [40] developed a multi-physics cloak using topologycurrent. The design employs a transformation multiphysics cloak

to achieve cloaking in arbitrary shapes, validated through simulations and experiments. Their method couples thermal and electric conductivities in a single device, demonstrating enhanced cloaking abilities for both heat and electric fields. The approach offers flexibility in shape, functionality, and robust performance across various scenarios. Kalkan et al. [41] optimized a mini-channeled cold plate for LIB thermal management using multi-objective optimization and ANOVA. They minimized battery temperature and coolant pressure drop, determining the optimal design parameters: a 5 mm channel width, a 5 mm branch distance, a 10 mm channel depth, 13 crossovers, and a 0.7061 l/min coolant flow. In addition, other studies have demonstrated the significant potential of machine learning, RSM, the Taguchi method, and ANOVA in assessing factors such as mass flow rate, channel number, and other key parameters [42,43]. Zuo et al. [44] developed an improved multi-channel cold plate for thermal management of $LiFePO_4$ batteries. They applied grey relational analysis, the Taguchi method, and ANOVA to evaluate factors such as mass flow rate, channel number, ambient temperature, and oblique angle. The optimal configuration achieved the lowest pressure drop and the highest j/f factor. This study highlights the potential of these methods in optimizing cold plate design.

Extensive literature reviews indicate that an ideal cold plate for BTMS should simultaneously offer minimal flow pressure drop and enhanced thermal performance. Achieving such an optimal design requires an accurate correlation between structural parameters and performance metrics, which can be realized through reliable multi-objective optimization methods. Furthermore, it is essential to explore practical and efficient structural designs suitable for BTMS applications. Manifold cold structures have been demonstrated to possess both high heat dissipation capacity and low flow resistance [18,45,46]. Although several studies have applied these structures to LIB cooling, most have focused on straight-channel configurations. The impact of varying channel geometries within manifold structures on BTMS performance remains insufficiently investigated. In addition, conventional machine learning approaches often demand large volumes of training data to achieve acceptable accuracy, which significantly increases computational cost and workload.

This study proposes a novel manifold cold plate structure featuring an overflow channel with a bottom triangular ridge, designed to enhance the thermal management performance of lithium-ion batteries. Compared to conventional straight-channel designs, the proposed structure offers significant advantages in reducing flow resistance and improving heat dissipation. To achieve optimal performance, a multi-objective optimization framework is developed by integrating RSM, NSGA-II, and the LINMAP decision-making method, enabling a precise trade-off between thermal performance and pressure drop. Furthermore, this work focuses on a practically significant yet underexplored scenario—a 1P52S configuration of 280 Ah $LiFePO_4$ batteries, widely used in energy storage systems [47]. The effectiveness and robustness of the optimized cold plate are validated through both steady-state and transient Computational Fluid Dynamics (CFD) simulations under various discharge rates, demonstrating its strong potential for practical application in battery thermal management systems.

2 Geometric Model and Numerical Method

2.1 Geometric Model of the BTMS

As shown in Fig. 1, a three-dimensional computational model of a LIB thermal management system incorporating a manifold cold plate was established to investigate its thermal and hydraulic performance. The battery module consists of 52 prismatic cells arranged in a 4 × 13 configuration. Each cell measures 72 mm in length (l_b), 174 mm in width (w_b), and 207 mm in height (h_b) [48]. The cold plate is installed beneath the battery module and adopts a manifold-type heat dissipation structure. A series of parallel overflow channels is arranged on the contact interface with the battery,

with triangular ridges designed at the bottom of each channel to optimize coolant flow distribution and enhance heat transfer performance. As illustrated in Fig. 1, the blue arrows indicate coolant flow within the inlet manifold channels, while the red arrows represent flow in the outlet manifold channels. The inlet and outlet manifold channels are arranged in an alternating pattern. The inlet manifold channels are sealed at their outlet ends, while the outlet manifold channels are sealed at their inlet ends, thereby forming a staggered and unidirectional flow path. This manifold configuration has been widely recognized for its advantages of low flow resistance and high heat dissipation efficiency [18,49,50]. During operation, the coolant first enters the system through a primary inlet manifold and is then distributed into the inlet manifold channels. It subsequently flows through the overflow channels, where the majority of heat exchange takes place. Finally, the fluid is directed into the outlet manifold channels and collected by the central outlet manifold for discharge. Notably, previous studies have demonstrated that conical channel geometries can enhance heat dissipation without significantly increasing flow resistance [46,51]. Therefore, in this study, a triangular ridge is incorporated at the bottom of each overflow channel to optimize both flow distribution and thermal performance. The detailed geometric parameters and thermal–physical properties used in the simulation are listed in Table 1.

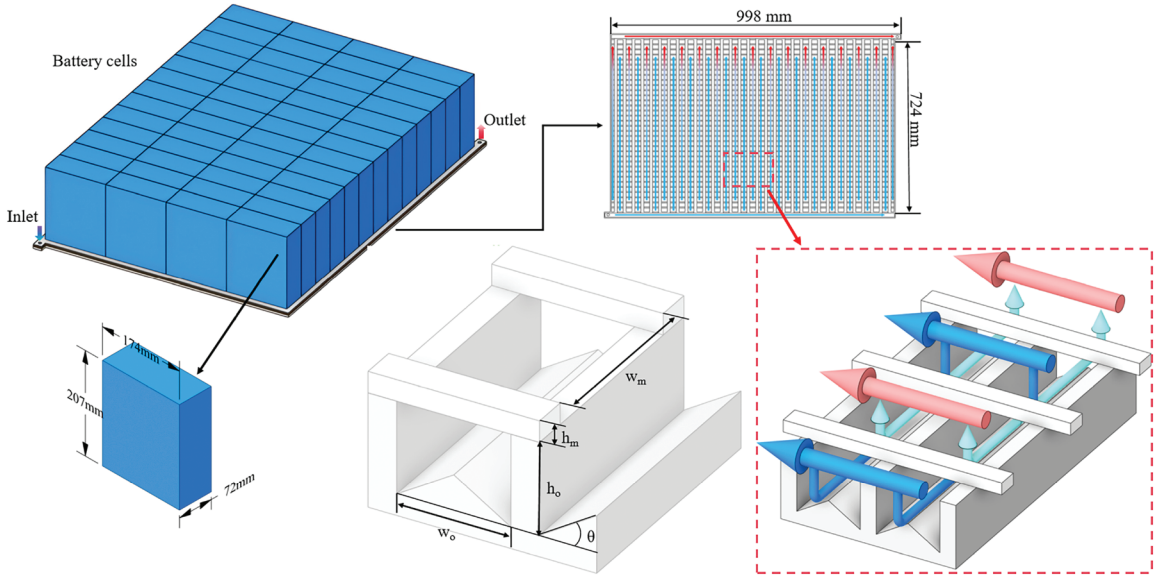

Figure 1: Geometric configuration of the battery pack and the manifold cold plate with triangular raised-bottom channels

Table 1: Summary of model parameters for the battery pack and cooling system

Componnent	Parameter	Value	Unit
Battery pack	$LiFePO_4$	280	Ah
	Size ($L_B \times W_B \times H_B$)	936 × 696 × 207	mm
Battery cell	Density	2300	kg/m^3
	Specific heat	967	J/(kg·K)
	Thermal conductivity	23.4 (k_x), 5.3 (k_y), 17.4 (k_z)	W/(m·K)
	Size ($l_b \times w_b \times h_b$)	174 × 72 × 207	mm

(Continued)

Table 1 (continued)

Componnent	Parameter	Value	Unit
Coolant	Density	1071.11	kg/m^3
	Viscosity	0.00339	Pa·s
	Specific heat	3300	J/(kg·K)
	Thermal conductivity	0.384	W/(m·K)
	Inlet velocity	1–2	m/s
	Inlet temperature	18	°C
Inlet	Inner diameter	8	mm
Overflow channel	Height (h_o)	2.4∼3	mm
	Width (w_o)	16	mm
Manifold channel	Height (h_m)	3∼3.6	mm
	Width (w_m)	6.66∼20	mm
Triangular ridge angle	θ	10∼30	°

2.2 Governing Equations and Boundary Conditions

Since the primary heat transfer within the cold plate occurs in the overflow channels, and the Reynolds numbers in these channels remain below 200, a laminar flow model is adopted throughout this study. To further simplify the numerical calculations, the following assumptions are made:

(1) The heat generation within each battery cell is assumed to be uniform.
(2) Thermal radiation is neglected in the simulation.
(3) The thermophysical properties of both the fluid and solid materials are considered constant and independent of temperature.
(4) The battery pack casing is assumed to have a negligible contribution to heat dissipation and is therefore excluded from the system-level optimization.

Under the assumptions above, the governing equations can be simplified in the way that follows [49,52]:

Continuity equation:

$$\frac{\partial \rho}{\partial t} + \frac{\partial u}{\partial x} + \frac{\partial u}{\partial y} + \frac{\partial u}{\partial z} = 0 \tag{1}$$

Momentum equation [53,54]:

$$\frac{\partial \rho u}{\partial t} + \rho u \cdot \nabla u = -\nabla p + \rho g + F \tag{2}$$

Energy equation [52]:

$$\frac{\partial}{\partial t}(\rho E) + \nabla \cdot (u(\rho E + p) = \nabla \cdot \left(k_{eff} \nabla T - \sum_i h_i J_i \right) + S \tag{3}$$

In the equations: u denotes velocity, E is the energy, ρ represents density, p stands for pressure, μ stands for the dynamic viscosity of the fluid, T represents temperature, c_p represents the specific heat capacity of the fluid, k signifies thermal conductivity, h is the enthalpy, J is the diffusion flux, S is the heat source term for battery cells.

The E and S could be calculated as follows [48]:

$$E = h - \frac{p}{\rho} + \frac{u^2}{2} \tag{4}$$

$$S = \frac{Q_b}{V_b} \tag{5}$$

where V_b is the volume of the battery, and Q_b is the heat generated by the battery during the charging or discharging process, which can be expressed as [55]:

$$Q_b = I^2 R - IT\frac{dV_{oc}}{dT} \tag{6}$$

where I is the current, R_i is the internal resistance, T is the battery temperature, and V_{oc} is the open-circuit voltage. During the discharging process of lithium-ion batteries, the internal resistance varies with the change in battery capacity, leading to a corresponding variation in heat generation. Therefore, accurately modeling the thermal behavior of the battery requires a reliable expression that captures the relationship between internal resistance and the depth of discharge (DoD). In this study, an empirical correlation (Eq. (7)) between the heat generation rate and the depth of discharge was obtained by fitting experimental data reported by Li et al. [47], providing a basis for thermal source modeling.

$$Q_b = 5398.6DOD^6 - 15860.1DOD^5 + 17667.2DOD^4 - 9146DOD^3 + 2202.7DOD^2 - 232.3DOD + 19.5 \tag{7}$$

As shown in Fig. 2, the fitted heat generation curve is compared with the experimental data. It can be observed that the simulation results exhibit a strong agreement with the experimental data across the entire range of DoD. The R^2 exceeds 0.98, indicating excellent fitting accuracy and demonstrating the reliability of the empirical correlation for thermal modeling purposes.

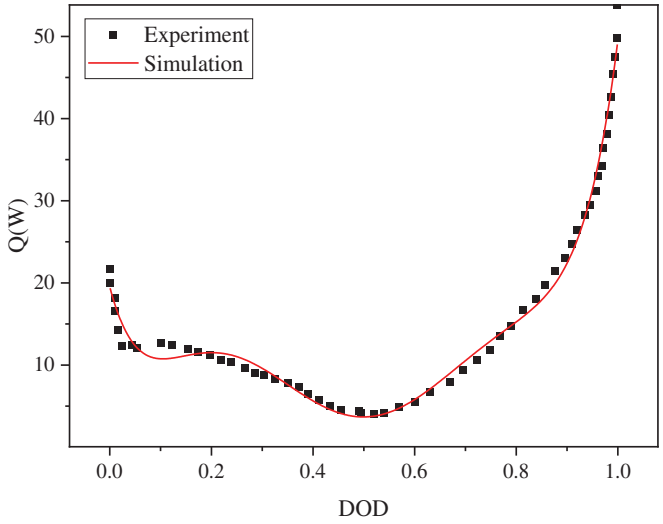

Figure 2: Comparison of simulated and experimental heat generation rates at various depths of discharge

2.3 Numerical Treatment

In this work, both transient and steady-state numerical simulations were carried out to investigate the thermal and fluid dynamic characteristics of the proposed BTMS. The volumetric heat generation is implemented into the governing equations through a User-Defined Function (UDF). Velocity-inlet and pressure-outlet boundary conditions were applied at the coolant inlet and outlet, respectively. The side walls of the computational domain were assigned a convective heat transfer coefficient of 5 W/(m^2·K). For steady-state simulations, a volumetric heat generation rate of 10 kW/m^3 was set for the representative battery cell. Convergence was considered to be achieved when either the outlet temperature stabilized or the residuals of the governing equations fell below 10^{-6}.

2.4 Grid Independence Verification

A grid independence study was conducted to ensure that the simulation results were not significantly affected by the mesh resolution, as shown in Fig. 3. The maximum battery temperature and the pressure drop between the inlet and outlet were selected as evaluation metrics. It can be observed that when the total number of elements exceeds 3.4 million, the variations in both maximum temperature and pressure drop become negligible. Therefore, a grid size of 3.4 million elements was adopted for all subsequent simulations.

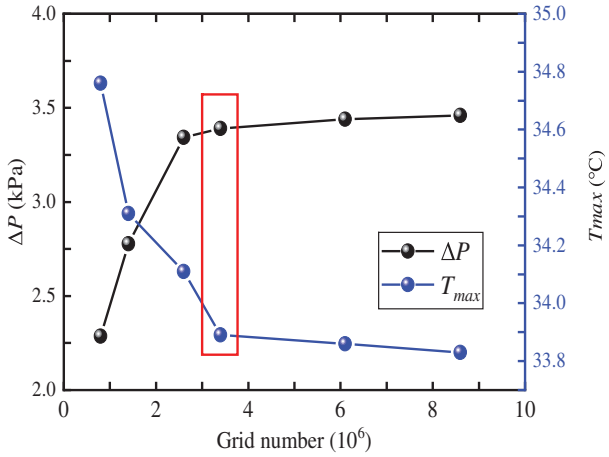

Figure 3: Grid independence study

3 Multi-Objective Optimization

3.1 Optimization Procedure

Fig. 4 illustrates the optimization framework used to enhance the thermal and hydraulic performance of the proposed liquid cooling plate. The process begins with the identification of key influencing factors and the formulation of multi-objective optimization goals. A Central Composite Design (CCD) method is then employed to generate simulation scenarios and systematically explore the design space. Next, multiple regression analysis is performed to develop empirical models that correlate the input variables with performance metrics. The statistical significance and adequacy of the regression models are evaluated using ANOVA. If the model fails to meet significance criteria, the regression modeling is revisited. Otherwise, response surface methodology is used to examine the trends and interactions among variables. Based on the established regression equations, the NSGA-II is used to derive a Pareto front that represents the trade-off between conflicting objectives. The LINMAP method is subsequently applied to determine the ideal solution from the Pareto-optimal set

by calculating the shortest Euclidean distance to the perfect point in the normalized objective space. Finally, the optimal design configuration corresponding to the recommended solution is extracted and used to guide system improvements. This multi-stage optimization approach ensures a balanced consideration of thermal efficiency and pressure drop within the battery thermal management system.

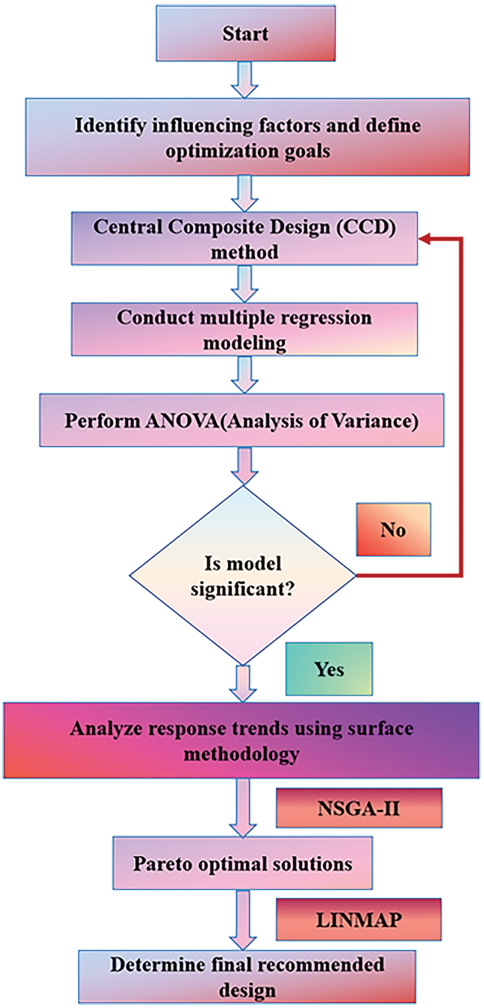

Figure 4: Multi-objective optimization framework for enhancing the thermal and hydraulic performance of the liquid cooling plate

3.2 Design Variables and Objective Functions

For the multi-objective optimization of the manifold liquid cooling plate, the ratio of inlet to outlet widths of the manifold channel ($\lambda = w_{m,in}/w_{m,out}$), the height ratio between manifold and overflow channels ($\phi = h_m/h_o$), the inlet velocity (u) and the inclination angle of the conical bottom surface in the overflow channel (θ) are selected as the key design variables. The optimization aims to achieve a balance between thermal and hydraulic performance. Therefore, the maximum temperature difference within the battery pack (ΔT_{cell}) and the pressure drop across the cold plate (Δp) are defined as the objective functions. The ranges and levels of the design variables used in the optimization process are listed in Table 2.

Table 2: The levels and actual values of the design parameters

Factor	Description	Coded levels		
		Level A	Level B	Level C
λ	Inlet-to-outlet width ratio of the manifold channel	1	2.5	5
ϕ	The height ratio between the manifold and overflow channels	1	1.25	1.5
u	inlet velocity	1	1.5	2
θ	Triangular ridge angle	10	20	30

3.3 Central Composite Design

Based on the CCD method and the selected design variables and levels, a total of 30 simulation cases were established, as presented in Table 3. The input variables include the inlet-to-outlet width ratio of the manifold channel (λ), the height ratio between the manifold and overflow channels (ϕ), the inlet velocity (u), and the Triangular ridge angle of the overflow channel bottom (θ). Through numerical simulations, the corresponding outputs were obtained for each case, including the maximum temperature difference of the battery pack (ΔT_{cell}) and the pressure drop between the inlet and outlet (Δp). These results provide the basis for subsequent regression modeling and multi-objective optimization analysis.

Table 3: CCD design matrix with simulation results

Test No.	λ	ϕ	u	θ	ΔT_{cell}	Δp
1	1	1	1	10	15.04	2752
2	5	1	1	10	15.53	2660
3	1	1.5	1	10	14.56	2977
4	5	1.5	1	10	15.72	3005
5	1	1	2	10	13.34	9869
6	5	1	2	10	13.47	9196
7	1	1.5	2	10	13.06	10,851
8	5	1.5	2	10	13.79	11,143
9	1	1	1	30	15.17	2700
10	5	1	1	30	15.45	2747
11	1	1.5	1	30	15.09	3313
12	5	1.5	1	30	15.54	3195
13	1	1	2	30	13.5	10,364
14	5	1	2	30	13.37	13,289
15	1	1.5	2	30	13.03	12,873
16	5	1.5	2	30	13.47	10,948
17	1	1.25	1.5	20	13.92	7105
18	3	1.25	1.5	30	13.62	5248
19	3	1	1.5	20	13.85	7209
20	3	1.5	1.5	20	13.94	7204
21	3	1.25	1.5	30	13.62	5248

(Continued)

Table 3 (continued)

Test No.	λ	ϕ	u	θ	ΔT_{cell}	Δp
22	3	1.25	2	20	13.23	13,126
23	3	1.25	1.5	30	13.62	5248
24	3	1.25	1.5	30	13.62	5248
25	3	1.25	1.5	20	13.93	7453
26	3	1.25	1.5	10	13.82	7031
27	3	1.25	1.5	30	13.62	5248
28	5	1.25	1.5	20	14.3	5510
29	3	1.25	1.5	30	13.62	5248
30	3	1.25	1	20	15.34	3344

3.4 Response Surface Methodology

RSM is a robust and widely applied statistical and mathematical technique designed to model and analyze problems in which a response of interest is influenced by several variables [56]. It is particularly effective for exploring the relationships between design parameters and performance objectives, especially in engineering optimization problems. The fundamental aim of RSM is to approximate the genuine functional relationship between the response and the design variables using a surrogate model, most commonly, a low-order polynomial. Compared to traditional methods such as the Taguchi technique or artificial neural networks, RSM exhibits superior accuracy, transparency, and computational efficiency, particularly when addressing thermodynamic and multi-physical challenges [57,58]. It achieves this by requiring a minimal number of experimental or simulation runs, thereby reducing the cost and complexity of the optimization process. In this study, a second-order polynomial regression model is adopted as the response surface function, which includes linear, quadratic (square), and two-factor interaction terms. The general form of the RSM model with n factors is expressed as [59]:

$$y = a_0 + \sum_{i=1}^{n} a_i x_i + \sum_{i=1}^{n} a_{ii} x_i^2 + \sum_{i=1}^{n} \sum_{i=1}^{n} a_{ij} x_{ij} + \varepsilon \tag{8}$$

where y is the predicted response, x_i and x_j are the independent design variables, a_0 is the intercept term, a_i is the coefficients of the linear terms, a_{ii} is the coefficients of the quadratic terms, a_{ij} is the coefficients of the interaction terms, ε is the random error term, respectively.

3.5 NSGA-II Algorithm

The NSGA-II is a widely adopted evolutionary algorithm for solving multi-objective optimization problems [43]. As illustrated in Fig. 5, the optimization process begins by randomly generating an initial population of candidate solutions, each of which is evaluated using the objective functions derived from the RSM. The population is then sorted into different non-dominated levels based on Pareto dominance. Within each front, a crowding distance metric is calculated to ensure diversity among solutions by favoring those in less populated regions of the design space. This strategy promotes uniform distribution along the Pareto front. Next, the algorithm adopts elitism to retain superior solutions for the next generation. Crossover and mutation operations are applied to selected individuals to generate offspring with new characteristics. The parent and offspring populations are

then merged and ranked again, from which a new population is formed for the next generation. These procedures are repeated iteratively until a predefined maximum number of generations is reached, at which point the algorithm outputs a set of non-dominated solutions. To avoid convergence to local optima, the NSGA-II algorithm incorporates genetic operators such as crossover and mutation to maintain population diversity. While crossover promotes local search by combining features from parent solutions, the mutation operator introduces new genetic material that is not present in the parents. This enables the algorithm to explore previously unvisited areas of the solution space. The stochastic nature of the mutation operator enables it to effectively escape local optima, thereby enhancing the global search capability of the algorithm [60].

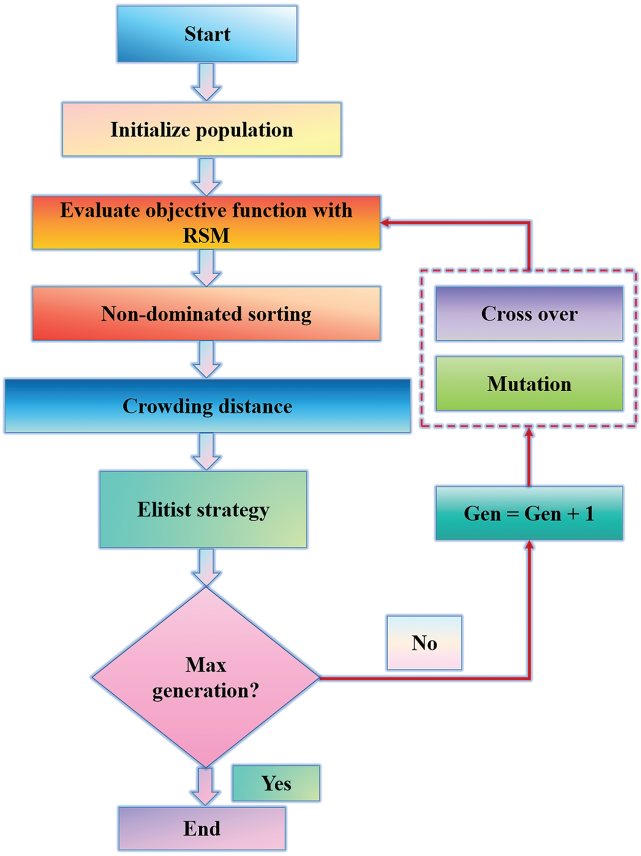

Figure 5: Flow chart of NSGA-II algorithm

3.6 LINMAP Decision-Making Method

Furthermore, selecting an appropriate decision-making strategy is essential for determining the most favorable solution among the Pareto-optimal set generated by multi-objective optimization. Among the available methods—such as TOPSIS, LINMAP, and fuzzy Bellman-Zadeh approaches—this study specifically adopts the LINMAP method, which determines the best solution based on its minimum distance to an ideal solution in the objective space.

In the LINMAP decision-making method, the final optimal solution (i_{LIN}) has a minimal distance from the ideal point as follows:

$$d_{i+} = \sqrt{\sum_{j=1}^{2} \left(F_{ij} - F_j^{ideal}\right)^2} \tag{9}$$

where F_{ij} represents the normalized value of the j_{th} objective for the i_{th} solution, and F_j^{ideal} denotes the ideal value of the j_{th} objective (typically the minimum or maximum value, depending on the optimization goal). The solution corresponding to the shortest distance is considered optimal:

$$i_{LIN} \equiv i \in \min\left(d_{i+}\right) \tag{10}$$

4 Results and Discussions

4.1 Validation of the Regression Model

To statistically validate the predictive performance of the developed regression model, ANOVA was performed for each response variable. ANOVA is a fundamental statistical technique for assessing the significance of model terms and quantifying the proportion of response variability that can be explained by the regression model [61].

Table 4 summarizes the statistical performance of the developed regression models for the output responses ΔT_{cell} and ΔP. The models exhibit strong goodness of fit, with both reactions achieving high R^2 of 0.9926 and 0.9600, respectively. The adjusted R^2 and predicted R^2 values for ΔT_{cell} are 0.9857 and 0.9534, indicating excellent model accuracy and predictive capability. For ΔP, the adjusted R^2 is 0.9227 and the predicted R^2 is 0.7735, which are acceptable for engineering applications. Additionally, the adequate precision values exceed the threshold of 4, further confirming the models' suitability for navigating the design space. The p-values for both models are less than 0.0001, suggesting that the fitted models are statistically significant and can be reliably used for subsequent optimization.

Table 4: ANOVA analysis for output responses

Response	Order	R^2	p-value	Adjusted R^2	Predicted R^2	Adequate precision
ΔT_{cell}	Quadratic	0.9926	<0.0001	0.9857	0.9534	38.2
ΔP	Quadratic	0.9600	<0.0001	0.9227	0.7735	14.8

To further verify the validity and significance of the developed regression models, a detailed analysis of the p-values and F-values corresponding to each regression coefficient was conducted, as presented in Table 5. The intercept terms (a_0) for ΔT_{cell} and ΔP exhibited high F-values (154.80 and 1091.03, respectively), confirming the overall significance of the models. Among the linear terms, a_2 (corresponding to u) and a_4 (corresponding to θ) showed consistently low p-values (< 0.05) and high F-values across all three responses, indicating that the fluid velocity and inlet temperature significantly influenced ΔT_{cell} and ΔP. In particular, a_4 exhibited extremely high F-values (1986.22 and 14,567.35 for ΔT_{cell} and ΔP, respectively), highlighting its dominant impact. For the interaction terms, a_{24} ($\phi \cdot \theta$) was found to be significant for ΔT_{cell} and ΔP, as evidenced by its low p-values (<0.05) and relatively large F-values. Additionally, a_{12} ($\lambda \cdot \phi$) and a_{23} ($\phi \cdot u$) demonstrated significant effects primarily on ΔP, suggesting that the interaction between design variables also played a non-negligible role in determining the system behavior. Regarding the quadratic terms, a_{11} (λ^2) and a_{44} (θ^2) exhibited statistical significance for ΔT_{cell} and ΔP, with p-values below 0.05 and noticeable F-values, further confirming the necessity of the quadratic terms in accurately capturing the nonlinear relationships

between the variables and responses. Overall, the analysis of *p*-values and F-values supports the conclusion that the key linear, interaction, and quadratic terms are statistically significant contributors to the predictive models. This further reinforces the validity, reliability, and robustness of the developed response surface models.

Table 5: *p*-value and F-value of ANOVA

Coefficient	ΔT_{cell} (°C) *p*-value	ΔT_{cell} (°C) F-value	ΔP (Pa) *p*-value	ΔP (Pa) F-value
a_0	–	154.80	–	1091.03
a_1	0.1157	2.79	<0.0001	32.92
a_2	0.0152	7.51	<0.0001	299.83
a_3	0.0005	19.15	<0.0001	43.07
a_4	<0.0001	1986.22	<0.0001	14,567.35
a_{12}	0.5022	0.4727	0.0042	11.33
a_{13}	0.3326	1	0.0119	8.18
a_{14}	0.7816	0.0797	0.0304	5.71
a_{23}	0.18	1.98	0.0034	12.1
a_{24}	0.0157	7.42	<0.0001	108.46
a_{34}	0.8551	0.0345	0.0381	5.17
a_{11}	0.0022	13.56	0.0936	3.21
a_{22}	0.8243	0.051	0.0438	2.82
a_{33}	0.9264	0.0088	0.1795	1.98
a_{44}	0.0021	13.79	<0.0001	57.81

To comprehensively assess the predictive performance of the developed models, scatter plots comparing the predicted values to the actual experimental results for ΔT_{cell} and ΔP are provided in Fig. 6. Each plot features a 45° reference line representing ideal agreement. As illustrated in Fig. 6a, the predicted values of ΔT_{cell} show excellent agreement with the actual data, confirming the high accuracy of the quadratic model in capturing thermal behavior. Similarly, Fig. 6b illustrates a strong correlation between the predicted and actual values of ΔP, with only minor deviations observed at higher pressures.

In addition to the R^2 and ANOVA analysis, further validation of the model adequacy was performed through comprehensive residual diagnostics, as illustrated in Fig. 7. The externally studentized residuals versus predicted plots (Fig. 7a,b) show that the residuals are randomly scattered around the zero line without any discernible patterns, suggesting that the assumptions of linearity and homoscedasticity are satisfied for the models predicting ΔT_{cell} and ΔP, respectively. The standard probability plots (Fig. 7c,d) demonstrate that the externally studentized residuals closely follow a straight line, indicating that the residuals are approximately normally distributed, which further supports the validity of the regression assumptions. The Cook's distance plots (Fig. 7e,f) were used to identify influential observations. All data points exhibit Cook's distance values well below the reference threshold of 1.0, confirming that no single experimental run unduly influences the model fits. Collectively, these diagnostic plots confirm that the developed quadratic response surface models are statistically adequate, robust, and suitable for subsequent multi-objective optimization.

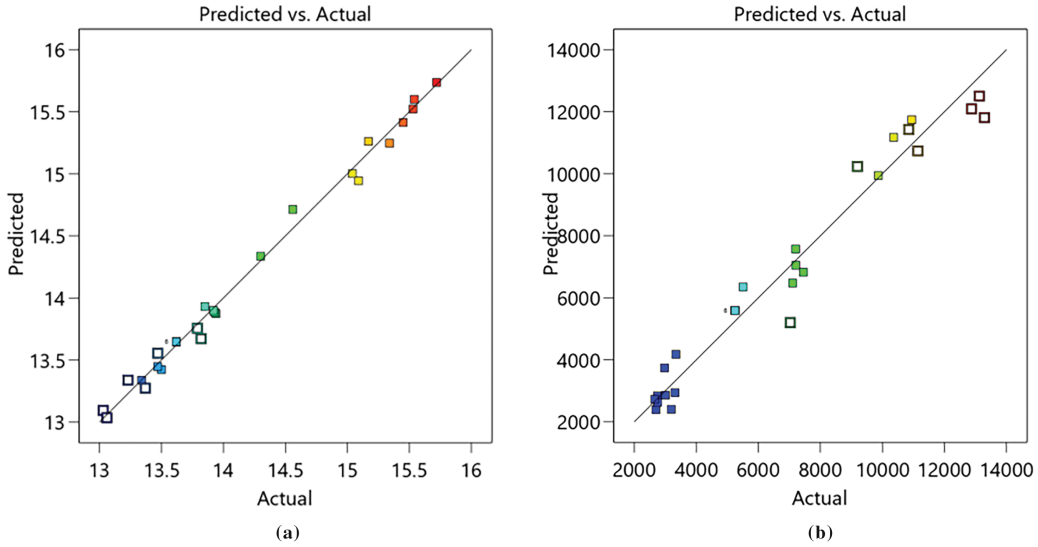

(a) (b)

Figure 6: Validation of model predictions for temperature rise and pressure drop: (**a**) ΔT_{cell}; (**b**) ΔP

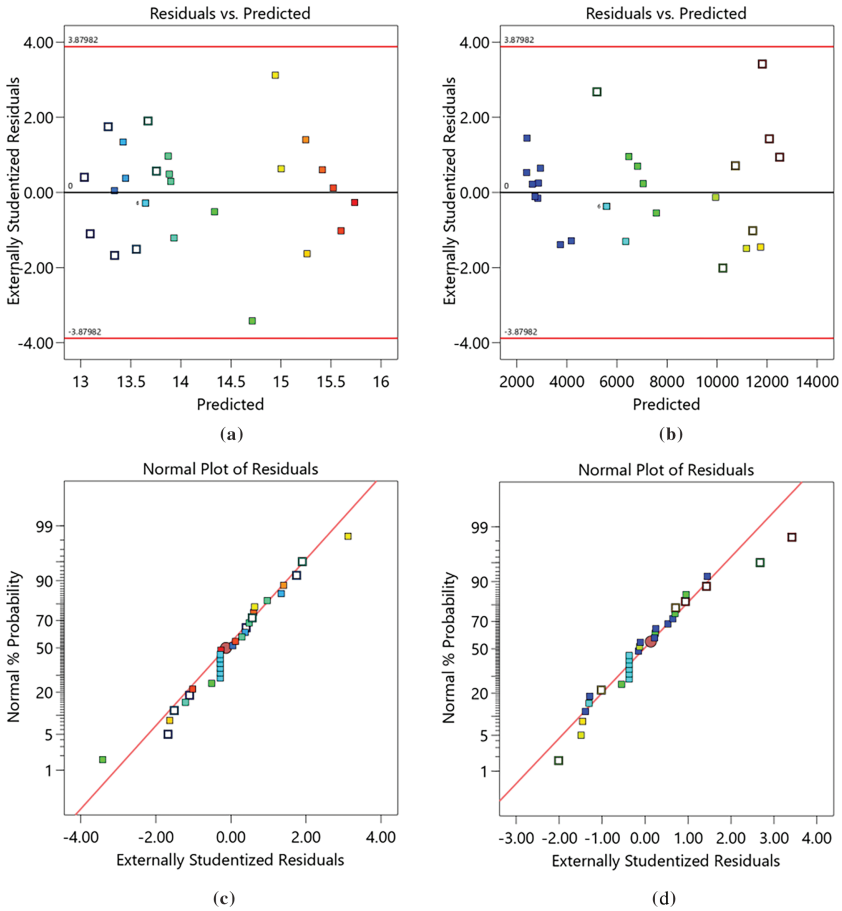

(a) (b) (c) (d)

Figure 7: (Continued)

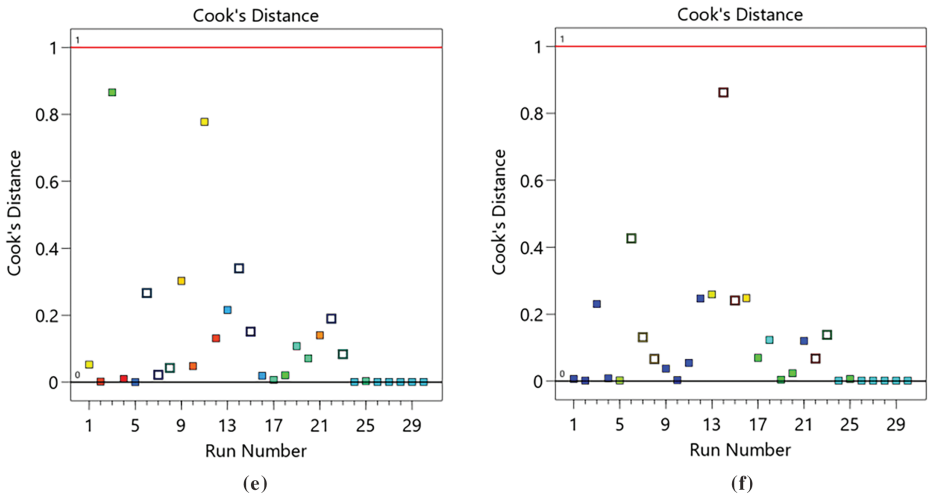

Figure 7: Comprehensive residual analysis of the regression models: (**a**) externally studentized residuals vs. predicted values of ΔT_{cell}; (**b**) externally studentized residuals vs. predicted values of ΔP; (**c**) normal probability plots of ΔT_{cell}; (**d**) normal probability plots of ΔP; (**e**) Cook's distance plots of ΔT_{cell}; (**f**) Cook's distance plots of ΔP

4.2 Response Function and Response Surface Analysis

Based on the constructed response surface models, two second-order polynomial regression equations have been established, as shown in Eqs. (11) and (12). By substituting specific values of the design variables into these predictive models, the corresponding response variables can be accurately evaluated.

$$\begin{aligned}\Delta T_{cell} = {} & 20.3011 - 0.3496\lambda - 1.5097\phi - 6.3781u + 0.1187\theta + 0.0583\lambda^2 + 0.2513\lambda\phi - 0.0756\lambda u \\ & - 0.0046\lambda\theta + 0.293\phi^2 - 0.0250\phi u - 0.0286\phi\theta + 1.6333u^2 - 0.0086u\theta - 0.0022\theta^2 \end{aligned} \tag{11}$$

$$\begin{aligned}\Delta P = {} & 12603.4254 + 1047.1011\lambda - 16855.5350\phi - 12357.8716u + 540.3834\theta - 103.4104\lambda^2 \\ & + 491.2500\lambda\phi - 47.1250\lambda u + 4.2938\lambda\theta + 7765.7362\phi^2 + 733.0000\phi u - 56.7500\phi\theta \\ & + 6055.4341u^2 + 73.1750u\theta - 14.3171\theta^2 \end{aligned} \tag{12}$$

To investigate the effects of λ, ϕ, u, and θ on the thermo-hydraulic performance of the manifold cold plate. Figs. 8 and 9 present the 3D response surfaces derived from the RSM-based regression models. As shown in Figs. 8 and 9, the u exerts the most significant influence on all thermal indicators. With increasing velocity, the convective heat transfer capability of the cold plate is enhanced, thereby improving heat dissipation efficiency and effectively reducing temperature gradients. However, this also results in a substantial rise in system pressure drop.

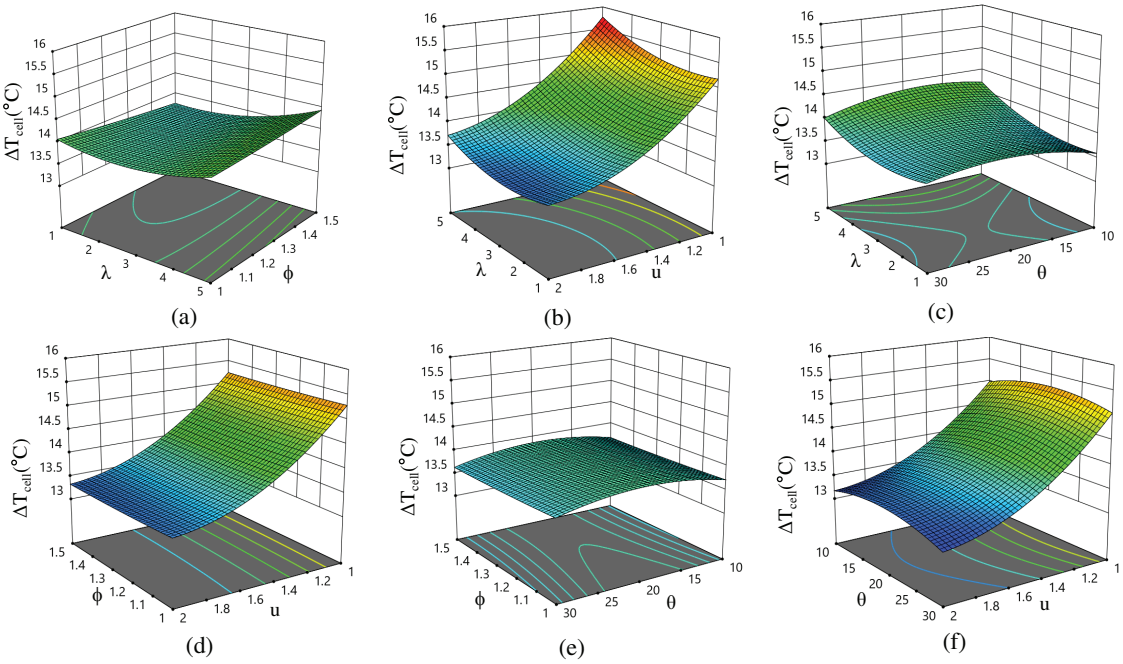

Figure 8: Response surface of the design parameter for ΔT_{cell} (**a**–**f**)

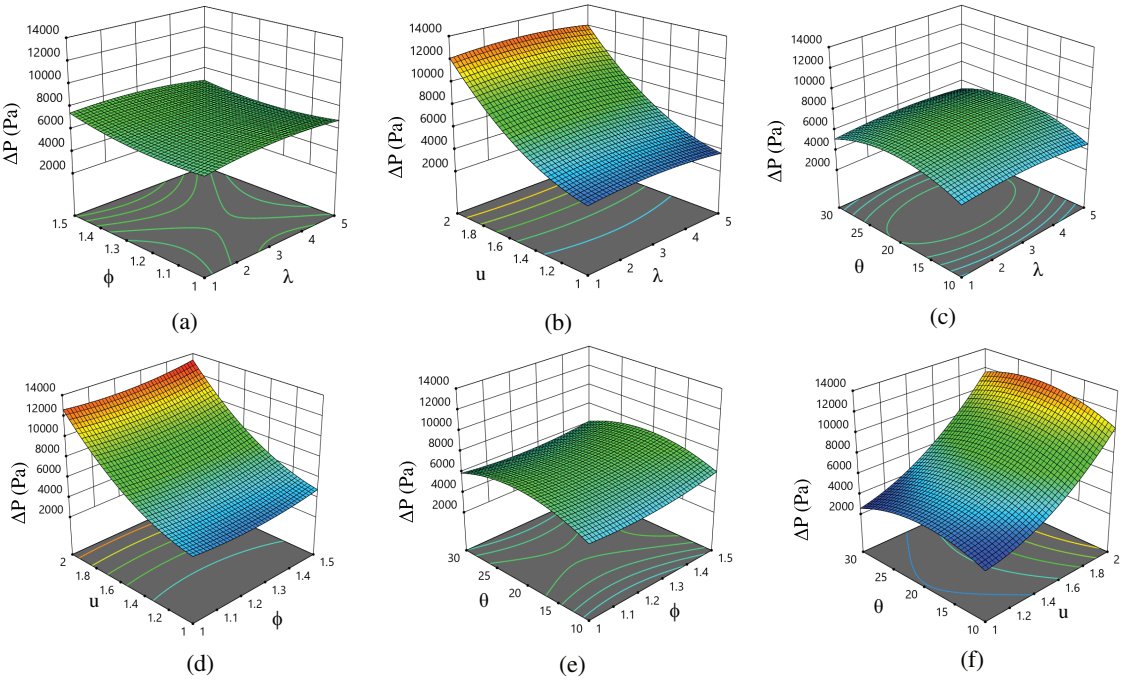

Figure 9: Response surface of the design parameter for ΔP (**a**–**f**)

In the analysis of ΔT_{cell}, u remains the most dominant factor. Higher inlet velocity enhances the overall heat removal capacity. It reduces local thermal accumulation within the battery pack,

resulting in a substantial decrease in the maximum temperature difference between cells. Although λ and ϕ exhibit relatively weak individual effects, their interaction with u still contributes to variations in thermal uniformity. A moderate increase in θ facilitates more favorable flow development within the overflow channel, enlarges the convective heat transfer area, and thereby enhances the cooling performance around the cells, ultimately lowering the peak temperature in the battery module. In contrast to thermal responses, the pressure drop ΔP is not only significantly affected by u but also highly sensitive to λ. A higher u inevitably increases system flow resistance, resulting in a steep rise in ΔP. Although increasing λ widens the inlet of the manifold channel, the simultaneous narrowing at the outlet contributes to a marked increase in local flow resistance. This conclusion is further supported by the ANOVA results shown in Fig. 9, where interaction terms such as λu and $\theta\phi$ exhibit p-values below 0.05, indicating statistically significant effects on both ΔP and ΔT_{cell}. These findings validate the interaction sensitivity observed in the response surface plots and emphasize the necessity of multi-parameter coupling in optimizing manifold cold plate design.

4.3 Optimization of Design Parameters

After establishing the response surface regression models and verifying their accuracy through numerical simulation, further exploration was conducted to identify optimal parameter combinations for the manifold cold plate design. In this section, a multi-objective optimization approach based on the NSGA-II is employed to achieve simultaneous improvement of thermal and hydraulic performance. The optimization objectives are to minimize the maximum temperature difference within the battery pack (ΔT_{cell}) and the pressure drop across the cold plate (ΔP). These two objectives are inherently conflicting, particularly about the inlet velocity, which affects them in opposing directions. The fitted response surface models for ΔT_{cell} and ΔP are used as the objective functions for the optimization process.

The design variables include the inlet-to-outlet width ratio of the manifold channel (λ), the height ratio between the manifold and overflow channels (ϕ), the inlet velocity (u), and the inclination angle of the conical overflow channel (θ). These variables are constrained within practical engineering ranges, as detailed in the following formulation:

$$\text{Minimize: } \Delta T_{cell} = y_1(\lambda, \phi, u, \theta)$$

$$\text{Minimize: } \Delta P = y_2(\lambda, \phi, u, \theta)$$

$$1 \leq \lambda \leq 5$$

$$1 \leq \phi \leq 1.5$$

$$1 \leq u \leq 2$$

$$10 \leq \theta \leq 30$$

The detailed design parameters used in the NSGA-II optimization algorithm are summarized in Table 6. To determine appropriate parameter values, multiple rounds of preliminary simulations were conducted by varying the population size (e.g., 50, 100, 150), generation number (e.g., 100, 200, 300), and control parameters for crossover and mutation. Through these iterative trials, a population size of 100 and a maximum generation count of 300 were selected to ensure sufficient solution diversity and convergence reliability. The crossover and mutation probabilities were finalized at 0.9 and 0.1, respectively, reflecting an optimal trade-off between exploration and exploitation observed during preliminary testing. In addition, the distribution indices for η_c and η_m were set to 15 and 20, respectively, based on their effectiveness in maintaining offspring diversity and controlling mutation intensity throughout the evolutionary process.

Table 6: Design parameters of NSGA-II

Parameter	Value
Population size	100
Maximum number of generations	300
Crossover probability	0.9
Mutation probability	0.1
Crossover distribution index (η_c)	15
Mutation distribution index (η_m)	20

Fig. 10 presents the Pareto front obtained from NSGA-II optimization, where the two conflicting objectives ΔP and ΔT_{cell} are simultaneously minimized. Each point on the Pareto front represents a non-dominated solution offering a trade-off between thermal uniformity and hydraulic performance. The lower-left corner marks the ideal point, corresponding to the theoretical minimum of both objectives. In Fig. 10, Point A, located in the upper-left region, exhibits excellent thermal performance but incurs a significant pressure drop. In contrast, Point B in the lower-right region minimizes pressure loss at the cost of an increased temperature difference. The selected point, identified using the LINMAP method, represents the optimal compromise solution, characterized by a pressure drop of approximately 6742.99 Pa and a corresponding temperature difference of 12.61°C.

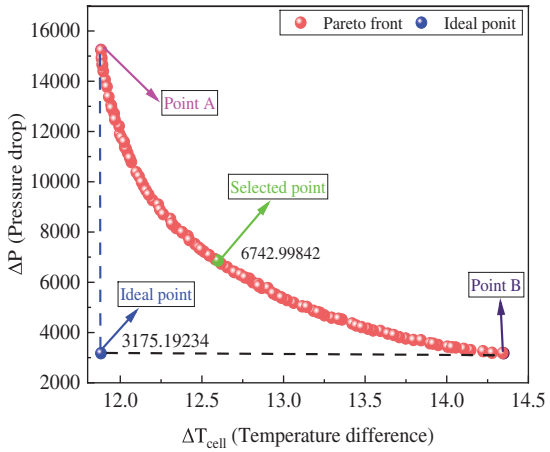

Figure 10: Pareto front for ΔT_{cell} and ΔP with LINMAP decision-making methods

To identify practical optimal solutions from the Pareto set, the two widely used LINMAP decision-making methods were applied. As shown in Table 7, the selected solution corresponds to the design parameters $\lambda = 1.031$, $\phi = 1.530$, $u = 1.671$ m/s, and $\theta = 29.8°$, resulting in $\Delta T_{cell} = 12.61$°C and $\Delta P = 6742.99$ Pa.

To assess the reliability of the NSGA-II optimization based on RSM surrogate models, the LINMAP optimal solution was re-evaluated using high-fidelity CFD simulations. As shown in Table 8, the CFD-predicted pressure drop and temperature difference are 6797.20 Pa and 12.96°C, respectively, compared to the RSM-based predictions of 6742.99 Pa and 12.60°C. The relative errors are 0.8% for ΔP and 2.8% for ΔT_{cell}, both within acceptable limits. These results confirm the high accuracy and

practical applicability of the surrogate models used in the optimization process, thereby validating the effectiveness of the proposed NSGA-II-based multi-objective design approach.

Table 7: Optimal results obtained from Ideal Point and LINMAP

Point	λ	ϕ	u (m/s)	θ (°)	ΔT_{cell} (°C)	ΔP (Pa)
A	2.263	1.499	1.99	29.99	11.22	15,216.53
B	1	1.115	1	29.98	14.35	3175.19
Selected point	1.031	1.47	1.671	29.800	12.61	6742.99
Ideal point	–	–	–	–	11.22	3175.19

Table 8: CFD validation of optimization results

Point	ΔP (NSGA-II)	ΔP (CFD)	Error	ΔT_{cell} (NSGA-II)	ΔT_{cell} (CFD)	Error
LINMAP	6742.99	6797.20	0.8%	12.60	12.96	2.8%

4.4 Cooling Performance of the Manifold Cold Plate under Various Discharge Rates

To more accurately evaluate the dynamic thermal response of the manifold cold plate under realistic battery operating conditions, a transient simulation was performed using time-dependent heat generation profiles, with parameters taken from Table 7. As shown in Fig. 11, under 1C discharge, the natural convection case exhibits the highest temperature rise, reaching 54.7°C, due to the absence of active cooling. Under the 1C discharge condition, the prototype configuration exhibits a slightly higher peak temperature of 43°C, while the LINMAP-optimized configuration reduces it to 41.68°C, indicating improved thermal control. At 0.5C discharge, a similar trend is observed with generally lower temperatures. The natural convection configuration reaches a maximum temperature of 39.29°C, whereas the prototype and LINMAP-optimized designs achieve 28.28°C and 27.5°C, respectively. Notably, the LINMAP-optimized configuration consistently maintains the lowest peak temperature across both discharge rates, highlighting its superior performance in enhancing thermal uniformity and mitigating thermal stress. Additionally, as shown in Fig. 11, the pressure drop of the LINMAP-optimized configuration is 6.797 kPa, only marginally higher than that of the prototype design (6.754 kPa).

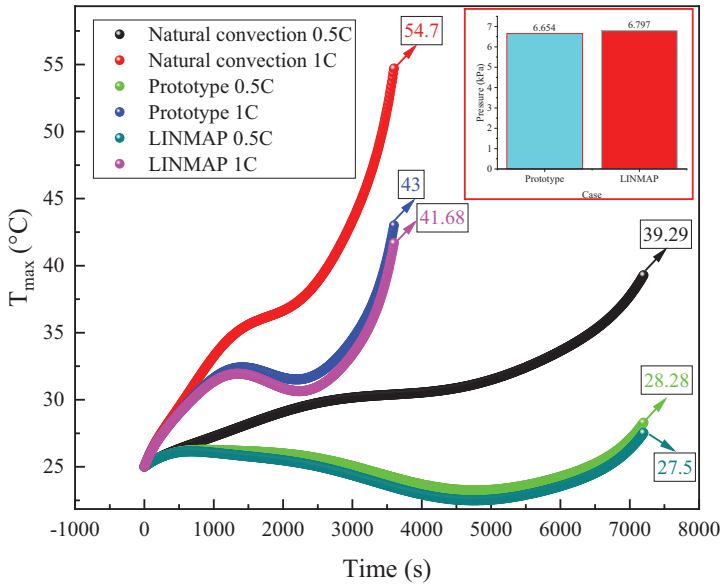

Figure 11: Transient thermal and hydraulic performance of natural convection, prototype, and LINMAP-optimized designs under 0.5 and 1C discharges

5 Conclusion

In this work, a manifold cold plate with triangular overflow channels was proposed and optimized for the thermal management of lithium-ion battery modules. ANOVA was employed to evaluate the reliability of the constructed regression models. The R^2 values for ΔT_{cell} and ΔP are 99.26% and 96.00%, respectively, indicating that the quadratic response surface models accurately capture the relationships between the design variables and the output responses. The corresponding F-values are 154.80 and 1091.03, with p-values less than 0.0001 for both models, confirming their high statistical significance. Sensitivity analysis revealed that the most influential parameters for ΔT_{cell} are, in descending order, the linear term of u, the linear term of θ, and their interaction term ($u{\cdot}\theta$). For ΔP, the most significant terms are the linear term of θ, the linear term of u, and the interaction term $\lambda{\cdot}\theta$. Quadratic terms such as θ^2 and λ^2 also showed significant effects on both responses. Response surface analysis further demonstrated that increasing the inlet velocity enhances convective heat transfer, thereby reducing ΔT_{cell}, but at the cost of increased ΔP. Similarly, a steeper channel bottom angle improves flow uniformity and thermal dispersion, while also contributing to higher pressure losses. Interaction effects between λ and u, as well as between θ and ϕ, were found to have statistically significant impacts on system performance. Multi-objective optimization was conducted using the NSGA-II algorithm to minimize ΔT_{cell} and ΔP simultaneously. The LINMAP method was then used to select the optimal design from the Pareto front. The configuration chosen achieved a ΔT_{cell} of 12.61°C and a ΔP of 6742.99 Pa, with design parameters $\lambda = 1.031$, $\phi = 1.47$, $u = 1.671$ m/s, and $\theta = 29.8°$. High-fidelity CFD validation showed good agreement with RSM predictions, with relative errors of 0.8% and 2.8%, respectively. Transient simulations under realistic discharge conditions further confirmed the effectiveness of the optimized design. Compared with the baseline prototype, the LINMAP-optimized configuration reduced peak temperatures across both 0.5 and 1C discharge rates, with only a marginal increase (0.6%) in pressure drop. This demonstrates

the proposed design's ability to enhance thermal uniformity while maintaining efficient hydraulic performance.

6 Practical Applications and Limitations

This study integrates CFD simulations, RSM, and the NSGA-II to establish an efficient multi-objective optimization framework aimed at improving the thermal and hydraulic performance of cold plates in liquid-cooled battery thermal management systems. The proposed approach significantly reduces the number of simulations required and enhances optimization efficiency, while effectively balancing the trade-off between maximum temperature difference and pressure drop.

However, this method has limitations. RSM may struggle with highly nonlinear or strongly coupled systems and is sensitive to sample distribution. High-dimensional problems require a large number of samples, which increases the cost. Moreover, the CFD models rely on idealized assumptions that may not reflect real-world conditions such as contact resistance and manufacturing variability. Future research will aim to address these limitations by incorporating experimental validation, more advanced surrogate models, and a broader range of practical boundary conditions.

Acknowledgement: None.

Funding Statement: This research was funded by Universiti Malaya under grant number MG029-2023.

Author Contributions: The authors confirm contribution to the paper as follows: Conceptualization, Hanwen Zhang, Poo Balan Ganesan; investigation and methodology, Hanwen Zhang, Wen Tong Chong; software, Hanwen Zhang; writing—original draft preparation, Hanwen Zhang, Poo Balan Ganesan; validation, Poo Balan Ganesan, Wen Tong Chong; data analysis and methodology, Mohd Nashrul Bin Mohd Zubir. All authors reviewed the results and approved the final version of the manuscript.

Availability of Data and Materials: The datasets generated and analyzed during the current study are available from the corresponding author on reasonable request.

Ethics Approval: Not applicable.

Conflicts of Interest: The authors declare no conflicts of interest to report regarding the present study.

References

1. Mikaeeli Kangarshahi B, Naghib SM, Younesian D, Rabiee N. Unlocking the rhythmic power of bacterial cellulose: a comprehensive review on green energy harvesting and sustainable applications. Adv Funct Mater. 2025;35(3):2413760. doi:10.1002/adfm.202413760.
2. Kumler A, Kravitz B, Draxl C, Vimmerstedt L, Benton B, Lundquist JK, et al. Potential effects of climate change and solar radiation modification on renewable energy resources. Renew Sustain Energy Rev. 2025;207(4):114934. doi:10.1016/j.rser.2024.114934.
3. Jafarizadeh H, Yamini E, Zolfaghari SM, Esmaeilion F, El Haj Assad M, Soltani M. Navigating challenges in large-scale renewable energy storage: barriers, solutions, and innovations. Energy Rep. 2024;12(3):2179–92. doi:10.1016/j.egyr.2024.08.019.

4. Kumar R, Lee D, Ağbulut Ü, Kumar S, Thapa S, Thakur A, et al. Different energy storage techniques: recent advancements, applications, limitations, and efficient utilization of sustainable energy. J Therm Anal Calorim. 2024;149(5):1895–933. doi:10.1007/s10973-023-12831-9.
5. Bin Abu Sofian ADA, Lim HR, Siti Halimatul Munawaroh H, Ma Z, Chew KW, Show PL. Machine learning and the renewable energy revolution: exploring solar and wind energy solutions for a sustainable future including innovations in energy storage. Sustain Dev. 2024;32(4):3953–78. doi:10.1002/sd.2885.
6. de Queiroz F Araújo O, Boa Morte IB, Borges CLT, Morgado CRV, de Medeiros JL. Beyond clean and affordable transition pathways: a review of issues and strategies to sustainable energy supply. Int J Electr Power Energy Syst. 2024;155:109544. doi:10.1016/j.ijepes.2023.109544.
7. Xu H, Shen M. The control of lithium-ion batteries and supercapacitors in hybrid energy storage systems for electric vehicles: a review. Int J Energy Res. 2021;45(15):20524–44. doi:10.1002/er.7150.
8. Galos J, Pattarakunnan K, Best AS, Kyratzis IL, Wang CH, Mouritz AP. Energy storage structural composites with integrated lithium-ion batteries: a review. Adv Mater Technol. 2021;6(8):2001059. doi:10.1002/admt.202001059.
9. Wiriyasart S, Hommalee C, Sirikasemsuk S, Prurapark R, Naphon P. Thermal management system with nanofluids for electric vehicle battery cooling modules. Case Stud Therm Eng. 2020;18(10):100583. doi:10.1016/j.csite.2020.100583.
10. Luo J, Zou D, Wang Y, Wang S, Huang L. Battery thermal management systems (BTMs) based on phase change material (PCM): a comprehensive review. Chem Eng J. 2022;430(9):132741. doi:10.1016/j.cej.2021.132741.
11. Zhao Y, Zhang X, Yang B, Cai S. A review of battery thermal management systems using liquid cooling and PCM. J Energy Storage. 2024;76(6):109836. doi:10.1016/j.est.2023.109836.
12. Hwang FS, Confrey T, Reidy C, Picovici D, Callaghan D, Culliton D, et al. Review of battery thermal management systems in electric vehicles. Renew Sustain Energy Rev. 2024;192(2):114171. doi:10.1016/j.rser.2023.114171.
13. Kausthubharam, Koorata PK, Panchal S, Fraser R, Fowler M. Investigation of the thermal performance of biomimetic minichannel-based liquid-cooled large format pouch battery pack. J Energy Storage. 2024;84(1):110928. doi:10.1016/j.est.2024.110928.
14. Vakilzadeh AH, Sarvestani AB, Javaherdeh K, Kamali R, Panchal S. Heat transfer and fluid flow in a PCM-filled enclosure: effect of heated wall configuration. J Energy Storage. 2024;87(12):111448. doi:10.1016/j.est.2024.111448.
15. Najafi Khaboshan H, Jaliliantabar F, Abdullah AA, Panchal S, Azarinia A. Parametric investigation of battery thermal management system with phase change material, metal foam, and fins; utilizing CFD and ANN models. Appl Therm Eng. 2024;247(13):123080. doi:10.1016/j.applthermaleng.2024.123080.
16. Xia G, Cao L, Bi G. A review on battery thermal management in electric vehicle application. J Power Sources. 2017;367(3):90–105. doi:10.1016/j.jpowsour.2017.09.046.
17. Tan X, Lyu P, Fan Y, Rao J, Ouyang K. Numerical investigation of the direct liquid cooling of a fast-charging lithium-ion battery pack in hydrofluoroether. Appl Therm Eng. 2021;196(1):117279. doi:10.1016/j.applthermaleng.2021.117279.
18. Yang H, Wang Z, Li M, Ren F, Feng Y. A manifold channel liquid cooling system with low-cost and high temperature uniformity for lithium-ion battery pack thermal management. Therm Sci Eng Prog. 2023;41:101857. doi:10.1016/j.tsep.2023.101857.
19. Larrañaga-Ezeiza M, Vertiz G, Arroiabe PF, Martinez-Agirre M, Berasategi J. A novel direct liquid cooling strategy for electric vehicles focused on pouch type battery cells. Appl Therm Eng. 2022;216:118869. doi:10.1016/j.applthermaleng.2022.118869.
20. Guo H, Li J, Zhu Z, Lv P. Numerical investigation on thermal performance of battery module with LCP-AFC cooling system applied in electric vehicle. Energy Sci Eng. 2022;10(12):4431–46. doi:10.1002/ese3.1275.

21. Osmani K, Alkhedher M, Ramadan M, Choi DS, Li LKB, Doranehgard MH, et al. Recent progress in the thermal management of lithium-ion batteries. J Clean Prod. 2023;389(5):136024. doi:10.1016/j.jclepro.2023.136024.
22. Liu H, Wei Z, He W, Zhao J. Thermal issues about Li-ion batteries and recent progress in battery thermal management systems: a review. Energy Convers Manag. 2017;150:304–30. doi:10.1016/j.enconman.2017.08.016.
23. Guo Z, Xu Q, Wang Y, Zhao T, Ni M. Battery thermal management system with heat pipe considering battery aging effect. Energy. 2023;263(1–2):126116. doi:10.1016/j.energy.2022.126116.
24. Saeedipour S, Gharehghani A, Rabiei M, Andwari AM, Mehranfar S, Reche CM, et al. Efficient BTMS for lithium-ion batteries: a study on PCM/metal foam, heat pipe, and microchannel integration. Transp Eng. 2025;20:100330. doi:10.1016/j.treng.2025.100330.
25. Akbarzadeh M, Kalogiannis T, Jaguemont J, Jin L, Behi H, Karimi D, et al. A comparative study between air cooling and liquid cooling thermal management systems for a high-energy lithium-ion battery module. Appl Therm Eng. 2021;198(2):117503. doi:10.1016/j.applthermaleng.2021.117503.
26. Shang Z, Qi H, Liu X, Ouyang C, Wang Y. Structural optimization of lithium-ion battery for improving thermal performance based on a liquid cooling system. Int J Heat Mass Transf. 2019;130:33–41. doi:10.1016/j.ijheatmasstransfer.2018.10.074.
27. Xu J, Chen Z, Qin J, Pan M. A lightweight and low-cost liquid-cooled thermal management solution for high energy density prismatic lithium-ion battery packs. Appl Therm Eng. 2022;203(8):117871. doi:10.1016/j.applthermaleng.2021.117871.
28. Qian Z, Li Y, Rao Z. Thermal performance of lithium-ion battery thermal management system by using mini-channel cooling. Energy Convers Manag. 2016;126:622–31. doi:10.1016/j.enconman.2016.08.063.
29. Han JW, Garud KS, Kang EH, Lee MY. Numerical study on heat transfer characteristics of dielectric fluid immersion cooling with fin structures for lithium-ion batteries. Symmetry. 2023;15(1):92. doi:10.3390/sym15010092.
30. Wang H, Tao T, Xu J, Mei X, Liu X, Gou P. Cooling capacity of a novel modular liquid-cooled battery thermal management system for cylindrical lithium ion batteries. Appl Therm Eng. 2020;178(2):115591. doi:10.1016/j.applthermaleng.2020.115591.
31. Rao Z, Zhang X. Investigation on thermal management performance of wedge-shaped microchannels for rectangular Li-ion batteries. Int J Energy Res. 2019;43(8):3876–90. doi:10.1002/er.4571.
32. Jarrett A, Kim IY. Design optimization of electric vehicle battery cooling plates for thermal performance. J Power Sources. 2011;196(23):10359–68. doi:10.1016/j.jpowsour.2011.06.090.
33. Jang DS, Yun S, Hong SH, Cho W, Kim Y. Performance characteristics of a novel heat pipe-assisted liquid cooling system for the thermal management of lithium-ion batteries. Energy Convers Manag. 2022;251(6–7):115001. doi:10.1016/j.enconman.2021.115001.
34. Lin XW, Shi MY, Zhou ZF, Chen B, Lu YJ, Jing DW. Multi-objective topology optimization design of liquid-based cooling plate for 280 Ah prismatic energy storage battery thermal management. Energy Convers Manag. 2025;325:119440. doi:10.1016/j.enconman.2024.119440.
35. Li D, Hu Q, Jiang W, Dong H, Song Z. Integrated power and thermal management for enhancing energy efficiency and battery life in connected and automated electric vehicles. Appl Energy. 2025;396(12):126213. doi:10.1016/j.apenergy.2025.126213.
36. Sui Z, Sui Y, Wu W. Multi-objective optimization of a microchannel membrane-based absorber with inclined grooves based on CFD and machine learning. Energy. 2022;240:122809. doi:10.1016/j.energy.2021.122809.
37. Fu Z, Zuo W, Li Q, Zhou K, Huang Y, Li Y. Multi-objective optimization of liquid cooling plate partially filled with porous medium for thermal management of lithium-ion battery pack by RSM, NSGA-II and TOPSIS. Energy. 2025;318(12):134853. doi:10.1016/j.energy.2025.134853.

38. Wanittansirichok V, Mongkholphan K, Chaowalitbumrung N, Sukjai Y, Promoppatum P. Topology optimization for liquid-based battery thermal management system under varied charge rates. J Energy Storage. 2022;55:105703. doi:10.1016/j.est.2022.105703.
39. Feng S, Shan S, Lai C, Chen J, Li X, Mori S. Multi-objective optimization on thermal performance and energy efficiency for battery module using gradient distributed Tesla cold plate. Energy Convers Manag. 2024;308(12):118383. doi:10.1016/j.enconman.2024.118383.
40. Zhu Z, Wang Z, Liu T, Xie B, Luo X, Choi W, et al. Arbitrary-shape transformation multiphysics cloak by topology optimization. Int J Heat Mass Transf. 2024;222:125205. doi:10.1016/j.ijheatmasstransfer.2024.125205.
41. Kalkan O, Celen A, Bakirci K. Multi-objective optimization of a mini channeled cold plate for using thermal management of a Li-Ion battery. Energy. 2022;251(1):123949. doi:10.1016/j.energy.2022.123949.
42. Dong H, Chen X, Yan S, Wang D, Han J, Guan Z, et al. Multi-objective optimization of lithium-ion battery pack thermal management systems with novel bionic Lotus leaf channels using NSGA-II and RSM. Energy. 2025;314(12):134226. doi:10.1016/j.energy.2024.134226.
43. Ren F, Li Q, Wang P. Multi-objective optimization of Tesla valve channel battery cold plate with nanofluid by RSM and NSGA-II. J Energy Storage. 2025;115:115969. doi:10.1016/j.est.2025.115969.
44. Zuo W, Zhang Y, Jiaqiang E, Huang Y, Li Q, Zhou K, et al. Effects of multi-factors on performance of an improved multi-channel cold plate for thermal management of a prismatic $LiFePO_4$ battery. Energy. 2022;261(39):125384. doi:10.1016/j.energy.2022.125384.
45. Chen Y, He M, Feng JC, Wang C, Zhuang Y. Thermal management performance of lithium-ion batteries coupled with honeycomb array manifold and phase change materials under microgravity conditions. Appl Therm Eng. 2024;251(1):123586. doi:10.1016/j.applthermaleng.2024.123586.
46. Zhang H, Ganesan P, Sharma RK, Bin Mohd Zubir MN, Badruddin IA, Chong WT. A novel overflow channel design of manifold cold plate for lithium-ion battery: a CFD study. Process Saf Environ Prot. 2024;189(3):648–63. doi:10.1016/j.psep.2024.06.092.
47. Li W, Wang Y, He B, Guo J, Ju G, Yu Z, et al. Influence of structural parameters on immersion cooling performance of a 1P52S 280 Ah prismatic $LiFePO_4$ battery pack. Appl Therm Eng. 2025;261(5):125185. doi:10.1016/j.applthermaleng.2024.125185.
48. Sui Z, Lin H, Sun Q, Dong K, Wu W. Multi-objective optimization of efficient liquid cooling-based battery thermal management system using hybrid manifold channels. Appl Energy. 2024;371:123766. doi:10.1016/j.apenergy.2024.123766.
49. Pan YH, Zhao R, Nian YL, Cheng WL. Numerical study on heat transfer characteristics of a pin-fin staggered manifold microchannel heat sink. Appl Therm Eng. 2023;219(11):119436. doi:10.1016/j.applthermaleng.2022.119436.
50. Husain A, Kim KY. Design optimization of manifold microchannel heat sink through evolutionary algorithm coupled with surrogate model. IEEE Trans Compon Packag Manuf Technol. 2013;3(4):617–24. doi:10.1109/TCPMT.2013.2245943.
51. Tang K, Lin G, Guo Y, Huang J, Zhang H, Miao J. Simulation and optimization of thermal performance in diverging/converging manifold microchannel heat sink. Int J Heat Mass Transf. 2023;200:123495. doi:10.1016/j.ijheatmasstransfer.2022.123495.
52. Pu X, Zhao Z, Sun M, Huang Y. Numerical study on temperature distribution uniformity and cooling performance of manifold microchannel heat sink. Appl Therm Eng. 2024;237(4):121779. doi:10.1016/j.applthermaleng.2023.121779.
53. Zhang S, Liu X, Wang E, Qian R, Wang M, Ma Q. A novel model of hydraulic aperture for rough single fracture: insights from fluid inertial and fracture geometry effects. J Geophys Res Solid Earth. 2024;129(7):e2024JB029018. doi:10.1029/2024JB029018.

54. Wu C, Qiu C, Yuan X, Yuan N, Zhang B, Li Y, et al. Numerical study and optimization of battery thermal management systems (BTMS) Based on Fin-Phase change material (PCM) in variable gravity environments. Appl Therm Eng. 2024;244:122777. doi:10.1016/j.applthermaleng.2024.122777.
55. Yang S, Li J, Cao B, Wu Z, Sheng K. Investigation of Z-type manifold microchannel cooling for ultra-high heat flux dissipation in power electronic devices. Int J Heat Mass Transf. 2024;218(10):124792. doi:10.1016/j.ijheatmasstransfer.2023.124792.
56. Bezerra MA, Santelli RE, Oliveira EP, Villar LS, Escaleira LA. Response surface methodology (RSM) as a tool for optimization in analytical chemistry. Talanta. 2008;76(5):965–77. doi:10.1016/j.talanta.2008.05.019.
57. Uslu S. Optimization of diesel engine operating parameters fueled with palm oil-diesel blend: comparative evaluation between response surface methodology (RSM) and artificial neural network (ANN). Fuel. 2020;276:117990. doi:10.1016/j.fuel.2020.117990.
58. Asghar A, Abdul Raman AA, Daud WM. A comparison of central composite design and Taguchi method for optimizing Fenton process. Sci World J. 2014;2014(4):869120. doi:10.1155/2014/869120.
59. Chi G, Hu S, Yang Y, Chen T. Response surface methodology with prediction uncertainty: a multi-objective optimisation approach. Chem Eng Res Des. 2012;90(9):1235–44. doi:10.1016/j.cherd.2011.12.012.
60. Dang DC, Friedrich T, Kötzing T, Krejca MS, Lehre PK, Oliveto PS, et al. Escaping local optima using crossover with emergent diversity. IEEE Trans Evol Comput. 2018;22(3):484–97. doi:10.1109/tevc.2017.2724201.
61. Armstrong RA, Eperjesi F, Gilmartin B. The application of analysis of variance (ANOVA) to different experimental designs in optometry. Ophthalmic Physiol Opt. 2002;22(3):248–56. doi:10.1046/j.1475-1313.2002.00020.x.